Optimization of the design of thick, segmented scintillators for megavoltage cone-beam CT using a novel, hybrid modeling technique

Langechuan Liu, Larry E. Antonuk,[a] Youcef El-Mohri, Qihua Zhao, and Hao Jiang
Department of Radiation Oncology, University of Michigan, Ann Arbor, Michigan 48109

(Received 12 November 2013; revised 11 April 2014; accepted for publication 22 April 2014; published 29 May 2014)

Purpose: Active matrix flat-panel imagers (AMFPIs) incorporating thick, segmented scintillators have demonstrated order-of-magnitude improvements in detective quantum efficiency (DQE) at radiotherapy energies compared to systems based on conventional phosphor screens. Such improved DQE values facilitate megavoltage cone-beam CT (MV CBCT) imaging at clinically practical doses. However, the MV CBCT performance of such AMFPIs is highly dependent on the design parameters of the scintillators. In this paper, optimization of the design of segmented scintillators was explored using a hybrid modeling technique which encompasses both radiation and optical effects.
Methods: Imaging performance in terms of the contrast-to-noise ratio (CNR) and spatial resolution of various hypothetical scintillator designs was examined through a hybrid technique involving Monte Carlo simulation of radiation transport in combination with simulation of optical gain distributions and optical point spread functions. The optical simulations employed optical parameters extracted from a best fit to measurement results reported in a previous investigation of a 1.13 cm thick, 1016 μm pitch prototype BGO segmented scintillator. All hypothetical designs employed BGO material with a thickness and element-to-element pitch ranging from 0.5 to 6 cm and from 0.508 to 1.524 mm, respectively. In the CNR study, for each design, full tomographic scans of a contrast phantom incorporating various soft-tissue inserts were simulated at a total dose of 4 cGy.
Results: Theoretical values for contrast, noise, and CNR were found to be in close agreement with empirical results from the BGO prototype, strongly supporting the validity of the modeling technique. CNR and spatial resolution for the various scintillator designs demonstrate complex behavior as scintillator thickness and element pitch are varied—with a clear trade-off between these two imaging metrics up to a thickness of ~3 cm. Based on these results, an optimization map indicating the regions of design that provide a balance between these metrics was obtained. The map shows that, for a given set of optical parameters, scintillator thickness and pixel pitch can be judiciously chosen to maximize performance without resorting to thicker, more costly scintillators.
Conclusions: Modeling radiation and optical effects in thick, segmented scintillators through use of a hybrid technique can provide a practical way to gain insight as to how to optimize the performance of such devices in radiotherapy imaging. Assisted by such modeling, the development of practical designs should greatly facilitate low-dose, soft tissue visualization employing MV CBCT imaging in external beam radiotherapy. [http://dx.doi.org/10.1118/1.4875724]

Key words: megavoltage cone-beam CT, flat-panel imager, electronic portal imaging device, hybrid modeling, Monte Carlo simulation, segmented crystalline scintillators, high x-ray detection efficiency, optimization

1. INTRODUCTION

In recent years, there has been increasing interest in improving the performance of the electronic portal imaging devices (EPIDs) used to visualize the megavoltage (MV) beam in radiotherapy treatment rooms. Presently, EPIDs are largely based on active matrix flat-panel imagers configured specifically for the megavoltage treatment beam (and are referred to as MV AMFPIs).[1] The technology typically consists of an x-ray converter comprising an ~1 mm thick copper sheet along with a relatively thick phosphor screen (e.g., 133 mg/cm^2 of gadolinium oxysulfide) that is optically coupled to a large area, active matrix, flat-panel array. The motivation for these improvement efforts is driven by the rather low x-ray detection efficiencies of conventional MV AMFPIs (~2%), resulting in detective quantum efficiencies of only ~1%.[2,3] The wide variety of approaches that have been explored for significantly improving detection efficiency and detective quantum efficiency (DQE) have been summarized in a number of publications.[1,4–7] These approaches employ both indirect and direct detection of the incident radiation—corresponding to use of scintillating and nonscintillating converters, respectively.

A particularly promising approach for increasing DQE involves replacement of the phosphor screen with thick, scintillating crystals. The crystals are arranged in the form of a two-dimensional matrix of optically isolated elements—with each element consisting of a scintillating crystal surrounded by

optically opaque septal wall material. Such *segmented scintillators* have been examined in numerous empirical[6,8–11] and theoretical[12–16] studies of various designs with crystal thicknesses ranging up to 4 and 6 cm, respectively. The use of segmented scintillators in early prototypes has, thus far, been shown to significantly increase DQE values up to levels of ~25%.[6,9,10]

The primary importance of such order of magnitude increases in DQE is that the dose necessary to capture a single projection image is greatly reduced. This, in turn, makes it possible to acquire the large number of images required to perform megavoltage cone-beam computed tomography (MV CBCT) at a clinically practical dose—comparable to that required to capture a single projection image with a conventional MV AMFPI.[10,11] Compared to kV CBCT images obtained in the treatment room, MV CBCT images exhibit significantly reduced streak artifacts for patients with metal implants.[17–19] In addition, CT-numbers obtained from MV CBCT can be more readily used for dose calculation in treatment planning.[20–22] Moreover, the fact that MV CBCT images are obtained using the therapy beam itself eliminates the type of geometric uncertainties relative to the treatment beam introduced by the use of an additional kV source and detector.

Toward the goal of realizing devices that offer maximum clinical benefit, it is of interest to examine how the performance of segmented scintillators can be improved through insights gained from theoretical modeling of potential designs.[6,9,12–15,23–25] Such modeling should account for both radiation and optical effects and an obvious approach would involve Monte Carlo based, event-by-event simulation of both radiation and optical transport so as to account for the most important physical effects.[13,23] However, since scintillation yields range from ~8000 to 54 000 optical photons per MeV of deposited x-ray energy for the most promising scintillators for this application ($Bi_4Ge_3O_{12}$ [BGO], $Lu_{1.8}Y_{0.2}SiO_5$ [LYSO], $CdWO_4$ and CsI:Tl),[26,27] the computational demands related to optical transport can greatly exceed those related to radiation transport. This, plus the fact that the number of x-ray histories required for such studies is itself often very large (so as to achieve clinically realistic doses or a desired level of statistical precision), means that studies can become too computationally burdensome to be carried out on practical timescales. One approach to circumvent this restriction is to simply reduce the scintillation yield, but this can be done only up to the point where deviations from results obtained with the nominal yield are within the tolerance of the study. For example, in a study of the optical Swank factor of segmented scintillators,[13] while it was possible to reduce the yield for CsI:Tl from 54 000 to 5400, no such reduction for BGO was feasible given the already relatively low yield (8000 photons/MeV) of this material.

In this paper, an examination of how variations in the design of BGO segmented scintillators affect imaging performance is reported. BGO was chosen due to the generally promising performance of previous prototype segmented scintillators incorporating the material, resulting from properties such as high electron density and refractive index, as well as a high degree of optical transparency.[6,11,26] The present investigation involves simulation of reconstructed images of a contrast phantom using a CBCT geometry at clinically realistic radiation doses—accounting for both radiation and optical transport effects. Given the very large number of x-ray histories required for the study, a purely event-by-event Monte Carlo modeling approach would have been computationally prohibitive even had the scintillation yield been reduced to a level consistent with avoiding deleterious effect on accuracy. For that reason, a novel hybrid modeling technique that reduced the computational time required to model various scintillator designs to a practical level was devised and implemented. This technique was used to evaluate the performance, in terms of contrast, noise, and contrast-to-noise ratio (CNR), of a variety of hypothetical designs. The technique was also used to examine the spatial resolution performance of those designs in terms of modulation transfer function (MTF). CNR is a widely accepted metric that is commonly employed for characterization of the performance of volumetric CBCT imaging systems employing AMFPIs.[11,12,28–34] MTF is a standard metric commonly employed for characterization of 2D imaging system spatial resolution performance. Improvements to system MTF resulting from adjustments to scintillator design are expected to lead to 3D spatial resolution improvement, the degree of which depends on the multitude of factors that affect the latter, as described in Sec. 4. Finally, a graphical method of combining CNR and MTF simulation results so as to provide further insight into design considerations that affect performance is introduced and discussed.

2. METHODS

2.A. Overview of converter designs and radiation simulation setup

Each segmented scintillator design examined in the study consists of a two-dimensional matrix of elements comprising rectangular cuboid shaped scintillator crystals separated by 0.05 mm thick, polystyrene septal walls. All designs employ BGO material with thicknesses ranging from 0.5 to 6 cm and element-to-element pitches ranging from 0.508 to 1.524 mm. The 0.5 cm lower limit on thickness corresponds to a point below which improvements in detection efficiency become marginal, whereas the 6 cm upper limit corresponds to a point beyond which the rate of improvement in detection efficiency as a function of thickness rapidly declines. The range chosen for pitch roughly brackets the range of spatial resolution of interest for therapy imaging.

For the CBCT simulation study, the scintillators have a detection area of ~70 × 140 mm^2 with pitches of 0.508, 0.762, 1.016, 1.270, and 1.524 mm, resulting in matrix formats of 141 × 281, 95 × 189, 71 × 141, 57 × 113, and 47 × 93, respectively. This detector area was chosen to be sufficiently large so as to allow imaging of the contrast phantom discussed below. For each scintillator, the radiation transport simulations included a 1 mm thick overlying layer of copper, representing the metal plate that is commonly used in MV portal imagers. Details of the setup are shown in Fig. 1 and a brief description follows. A point x-ray source, simulating a 6 MV

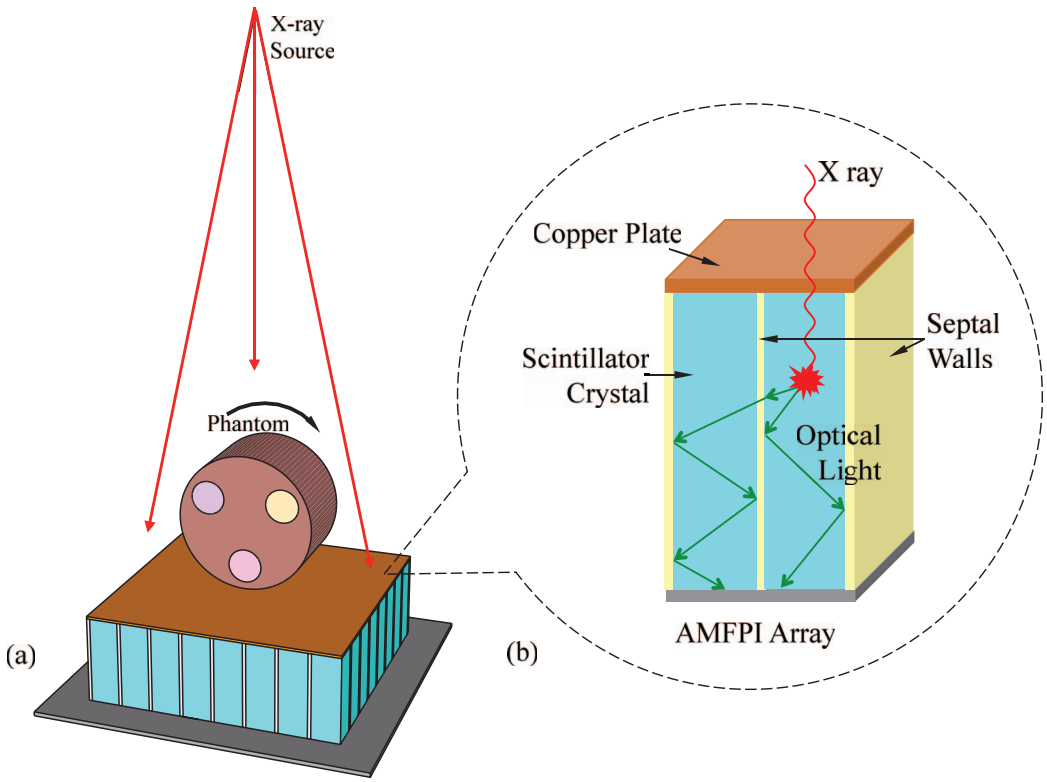

FIG. 1. (a) Schematic illustration of the setup employed in the CBCT simulations, including the x-ray converter and contrast phantom. The x-ray converter consists of a copper plate and a regular, two-dimensional matrix of elements (comprising scintillator and septal wall material) which are registered to the pixels of an underlying, indirect detection AMFPI array. (b) Enlarged view of the scintillator elements illustrating the physical process of energy deposition as well as of generation and transport of optical photons.

photon beam with a spectral output corresponding to that of a Varian radiotherapy linear accelerator[35] and located 130 cm away from the scintillator, was used. A contrast phantom with dimensions, composition, and inserts similar to those of an actual phantom used in a previous empirical MV CBCT study[11] was simulated. The phantom was positioned above the scintillator with its center at a distance of 124.2 cm from the source. It consists of an 11.4 cm diameter solid water cylinder with three cylindrical inserts, all having a common length of 6 cm. A total of 12 different inserts, each having a diameter of 2.8 cm, were simulated, resulting in four different phantom imaging configurations. The designations and physical properties of these materials are summarized in Table I. In the simulations, the x-ray fluence (i.e., the number of x rays per unit area) incident on the phantom per tomographic scan was set to a value of 4.32×10^7 x rays/mm^2 at a SDD of 130 cm. This value was determined through separate simulations in such a way as to provide a dose equivalent to the 4 cGy used in the previous empirical CBCT study—thereby facilitating direct comparisons with those results.

For the radiation transport part of the MTF simulation study, the spatial resolution for each scintillator design was characterized in terms of the presampled MTF, using the angled slit technique.[6,9,36] The simulation method used to determine MTF follows that reported in Ref. 15 and is briefly summarized as follows. Each design was simulated as a matrix of 101 × 101 scintillator elements with an overlying, 1 mm thick, copper plate located at a distance of 130 cm from an x-ray point source. The slit was modeled as a fan beam of 6 MV incident x rays, defining an aperture, centered along the central beam axis, of 10.26 cm × 4 μm at the detector

TABLE I. List of designations, densities, and electron densities relative to water for the tissue-equivalent materials of the simulated contrast phantom examined in this study. In these simulations, the composition and physical properties of each of the materials correspond to those of the actual phantom used in a previous empirical study (Ref. 11)—as provided by the manufacturer (Tissue Characterization Phantom, Gammex 467, Gammex rmi, Middleton, WI). Note that there are two entries for solid water material: one for the material comprising the main body of the phantom, and another for one of the tissue-equivalent inserts.

Designation of tissue-equivalent materials	Density (g/cm^3)	Electron density relative to water
Lung (LN-300)	0.29	0.280
Lung (LN-450)	0.44	0.429
Adipose (AP6)	0.94	0.925
Breast	0.98	0.954
Solid water (insert)	1.017	0.988
Solid water (phantom)	1.046	1.016
Brain	1.053	1.049
Liver (LV1)	1.097	1.065
Inner bone	1.143	1.096
Bone (B200)	1.154	1.106
Bone (CB2-30% mineral)	1.335	1.280
Bone (CB2-50% mineral)	1.56	1.470
SB3 cortical bone	1.825	1.697

entrance surface. The longer dimension of the slit was oriented at a small, fixed angle of 2° with respect to one direction of the matrix of scintillator elements. For each MTF simulation, 4×10^5 primary x-ray histories were employed—sufficient to keep statistical error below 0.9%.

2.B. Hybrid modeling technique

Simulation of the reconstructed CBCT images of the contrast phantom and of MTF was performed using a hybrid modeling technique. For each scintillator design, the technique entails a sequential process. First, projection radiation images are obtained from radiation transport simulation. Next, to account for the stochastic noise associated with energy-to-light conversion and detection, optical Swank noise,[37] deduced from optical gain distributions obtained from optical transport simulation, is added to those images. Finally, to account for spatial spreading of optical photons, optical blur is introduced through convolution of the noise-corrected images with an optical point spread function (PSF) that is obtained from the same optical transport simulation. A flowchart illustrating the implementation of the modeling technique is shown in Fig. 2 and a description of the various steps follows.

The Monte Carlo simulations of radiation transport were performed using the EGSnrc code.[38] In the simulations, the geometry of the scintillators and the contrast phantom were modeled using the EGSnrc C++ class library (egspp) (Ref. 39)—with the user code, as well as the input file that

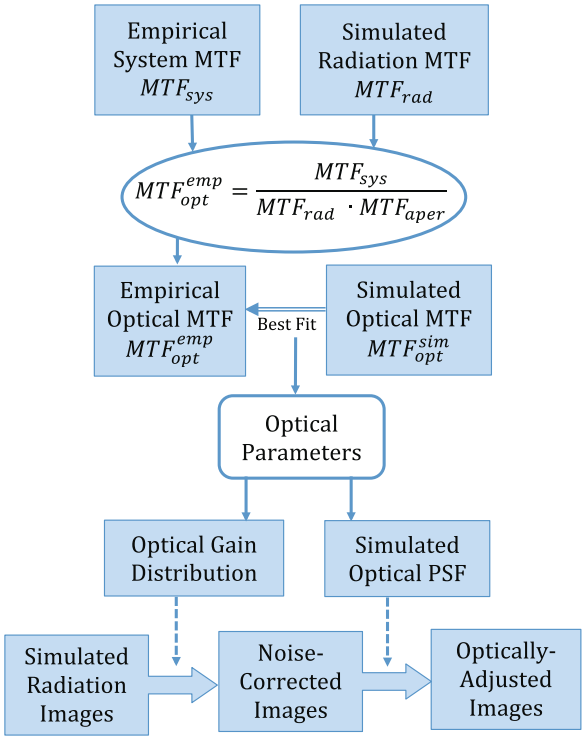

FIG. 2. Flowchart illustrating the hybrid modeling technique used to determine the CBCT and MTF performance of various scintillator designs. The lower half of the chart depicts how, for each scintillator design, optical effects are introduced using a simulated optical gain distribution and PSF. The upper half of the chart depicts how the optical parameters used to simulate the optical gain distributions and PSFs are obtained. See main text for details.

defines the geometry, modified as necessary. In the simulations, the cutoff energies for photons and electrons were set to 0.01 and 0.521 MeV, respectively, corresponding to a kinetic energy of 0.01 MeV. The EXACT boundary-crossing algorithm, PRESTA-II electron-step algorithm, and NIST bremsstrahlung cross sections were also used. The simulations were performed on a 64-bit Linux cluster with ~800 processor cores (4.0 GHz AMD FX Series).

The optical gain distribution and PSF for each design were also obtained through Monte Carlo simulation. These simulations employed optical parameters extracted from fits to published empirical MTF results for a 1.13 cm thick, 1.016 mm pitch prototype BGO segmented scintillator with septal walls consisting of 0.05 mm thick polymer reflector.[6] For the determination of these parameters, the expression representing the MTF of the system

$$\mathrm{MTF}_{\mathrm{sys}} = \frac{\mathrm{MTF}_{\mathrm{rad}} \times \mathrm{MTF}_{\mathrm{opt}}}{\mathrm{MTF}_{\mathrm{aper}}}, \quad (1)$$

is based on an expression from Ref. 3, where the system MTF is assumed to consist of radiation, optical, and aperture components. In Eq. (1), $\mathrm{MTF}_{\mathrm{rad}}$, $\mathrm{MTF}_{\mathrm{opt}}$, and $\mathrm{MTF}_{\mathrm{aper}}$ represent the radiation MTF, the optical MTF, and the aperture sinc function corresponding to the aperture defined by the cross-sectional size of the crystal of a scintillator element, respectively. Compared to the expression in Ref. 3, Eq. (1) takes a slightly different (though mathematically equivalent) form by deliberately including the contribution of $\mathrm{MTF}_{\mathrm{aper}}$ into both $\mathrm{MTF}_{\mathrm{rad}}$ and $\mathrm{MTF}_{\mathrm{opt}}$—a convention adopted for convenience given that this quantity is naturally embedded in all MTFs simulated in this study. The optical parameters were determined by fitting a simulated optical MTF, $\mathrm{MTF}_{\mathrm{opt}}^{\mathrm{sim}}$, to an empirically based optical MTF, $\mathrm{MTF}_{\mathrm{opt}}^{\mathrm{emp}}$. $\mathrm{MTF}_{\mathrm{opt}}^{\mathrm{emp}}$ itself was determined using Eq. (1) with values for $\mathrm{MTF}_{\mathrm{sys}}$, $\mathrm{MTF}_{\mathrm{rad}}$, and $\mathrm{MTF}_{\mathrm{aper}}$ obtained from previously published empirical results for the prototype, radiation transport simulation of that scintillator, and calculation, respectively.

The simulation of $\mathrm{MTF}_{\mathrm{opt}}^{\mathrm{sim}}$ was based on Monte Carlo techniques involving use of the optical simulation capabilities of Geant4.[40] Optical photons were generated within a narrow volume of the scintillator having a cross-sectional area corresponding to the slit used in the radiation transport part of the MTF simulations. While the photons were generated uniformly across that area, they followed a characteristic probability distribution in the depth direction that was based on the depth profile of the radiation energy deposited in the prototype scintillator. In those simulations, the interaction of optical photons with surfaces that separate neighboring media dominates optical spreading in the scintillator, since absorption and scattering in the scintillator crystal are negligible given the high degree of transparency of BGO.[41] The types of boundary interactions that could occur are included in Fig. 3 which represents a flowchart of the optical simulation steps. Briefly, at each boundary, there are four possible outcomes for a given photon (absorption, total internal reflection, transmission, or reflection) and the probability for each outcome is controlled by three parameters—absorptivity (α),

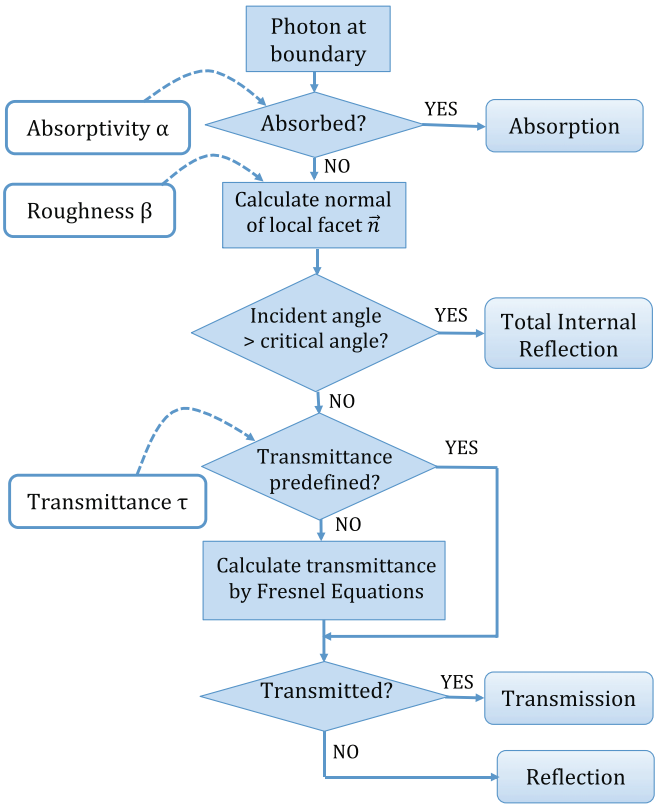

FIG. 3. Flowchart illustrating the logic applied to the consideration of the various boundary processes involved in the optical transport simulations. The sequence of decisions corresponds to the program structure of the optical simulation code in Geant4. The parameters that could, in principle, be used to characterize each boundary in the optical model are indicated on the left while the four possible outcomes are on the right. Note that, in the code, the value of transmittance can either be predefined or calculated using Fresnel equations.

roughness (β), and transmittance (τ). The set of values for these parameters that provided the best fit to the empirical results were subsequently used to simulate (also using Geant4) the optical gain distribution and PSF for each of the hypothetical scintillator designs.

For each hypothetical scintillator design, the simulation of the optical gain distribution and PSF involved the generation of optical photons inside the central element of a segmented scintillator consisting of 101 × 101 elements. A simulation consisting of 10 000 runs, with each run using 10 000 optical photon histories, was performed for a given design. While the photons were generated uniformly across the area of the crystal in the central element, they followed the radiation energy deposition profile for the corresponding scintillator in the depth direction. Following their transport through the scintillator, those optical photons exiting the bottom surface of the scintillator were recorded and that information was used as follows. In order to account for optical Swank noise in the radiation images, a histogram of the total number of recorded exiting photons per run, representing the optical gain distribution, was formed. For each scintillator element of each radiation image, this distribution, with a mean value μ and a standard deviation σ, was scaled according to the actual number of optical photons generated from the radiation energy deposited in that element (i.e., the radiation signal), using the following expressions for the mean value, μ_{sc}, and standard deviation, σ_{sc}, of the scaled distribution:

$$\mu_{sc} = \mu \frac{q\eta}{N_0}, \quad \sigma_{sc} = \sigma \sqrt{\frac{q\eta}{N_0}}. \tag{2}$$

In these expressions, q is the signal value in the radiation image, η is the energy-to-light conversion gain (8000 photons per MeV for BGO), and N_0 is the number of optical photons used in each simulation (10 000). For each element, random sampling was performed according to the corresponding scaled distribution to convert the radiation signal to a new signal value, resulting in an optical, noise-corrected image. In order to account for optical blur, the recorded exiting photons across all 10 000 runs were binned according to the element pitch to produce a discrete optical PSF which was convolved with the noise-corrected image to form the final, optically-adjusted image.

The inclusion of optical effects through use of a simulated optical gain distribution and PSF, as opposed to directly simulating the transport of the individual optical photons generated by each x ray interacting in the scintillator, consolidates the computation burden of optical transport simulations to a single optical simulation per design. This resulted in a significant reduction in the computation time required for the optical simulations from an estimated 10^8–10^{10} CPU hours to only ~30 CPU hours per design. As a result, whereas the present study would have required a total of $\sim 10^{11}$ CPU hours (dominated by optical transport simulation for the CBCT study), only $\sim 3.3 \times 10^6$ CPU hours (dominated by radiation transport simulation for that study) was required.

2.C. Determination of performance metrics: Contrast, noise, CNR, and MTF

For the CBCT simulation study, for each phantom imaging configuration and scintillator design, 180 projection radiation images were obtained by scanning the phantom tomographically with 2° angular increments over a 360° rotation. Separately, a set of 180 flood radiation images was obtained in the absence of the phantom, each using the same dose as that used for the individual projection images of the phantom. All radiation images were adjusted to include optical Swank noise and optical blur. A Feldkamp-based algorithm employing a ramp filter was used to reconstruct the spatial distribution of attenuation coefficients of the phantom from a combination of the set of adjusted projection images and the average of the 180 adjusted flood images.[12] The reconstructed voxel pitch and single slice thickness were chosen to be equal to the element pitch of the scintillator design. From the reconstructed tomographic images, a suitable number of consecutive single slices were averaged so as to provide a slice thickness of ~5 mm, irrespective of the element pitch. All reconstructed images were subject to a cupping artifact correction to remove a background trend due to beam hardening.[12]

Performance of the various scintillators was characterized in terms of contrast (*Contrast*), noise (*Noise*), and contrast-to-noise ratio (CNR) of the tissue-equivalent inserts relative to

the water-equivalent background in the reconstructed images of the contrast phantom. The analysis methods closely follow those used in a previous study.[11] In brief, the contrast of a given insert was calculated in Hounsfield units (HU) using the equation

$$\text{Contrast} = \frac{S_{\text{obj}} - S_{\text{water}}}{S_{\text{water}}} \times 1000\,(\text{HU})\,, \tag{3}$$

where S_{obj} and S_{water} represent the mean signal in the insert and water-equivalent regions, respectively. The signal for each insert is taken from a region consisting of an inner circle of ~14.2 mm diameter that excludes the edge of the insert while the signal for the background includes regions between the inserts, excluding the edges and center of the phantom. Similarly, the noise in the inserts was calculated using the equation

$$\text{Noise} = \frac{\sigma_{\text{obj}}}{S_{\text{water}}} \times 1000\,(\text{HU})\,, \tag{4}$$

where σ_{obj} represents the standard deviation of the signal in the inserts. CNR was calculated using

$$\text{CNR} = \frac{S_{\text{obj}} - S_{\text{water}}}{\sigma_{\text{obj}}}. \tag{5}$$

For the MTF simulation study, for each scintillator design, an image frame of energy deposited in the scintillator crystals by the angled radiation slit was obtained. This image was adjusted to include optical Swank noise and optical blur. From this adjusted image, a line spread function was determined using the angled-slit technique, the 1D Fourier transform of which yielded the MTF. Note that the analysis methods described above were also used to obtain CNR and MTF results in the absence of optical effects—results which are referred to as "radiation-only."

3. RESULTS

3.A. Determination of optical parameters

A list of the various optical parameters that could, in principle, be employed in optical simulation of interactions of photons with the top, side, and bottom surfaces of the elements of the segmented scintillator is given in Table II. For the present study, the top surface parameters were specified so as to correspond to either a black or a mirror top reflector (black: $\alpha_{\text{top}} = 1$; mirror: $\alpha_{\text{top}} = 0$, $\tau_{\text{top}} = 0$)—representing the reflectors employed in the previous empirical study.[6] In addition, transmittance for the sidewall and bottom surfaces, τ_{side} and τ_{bot}, were calculated using Fresnel Equations[42] employing the refractive index values appearing in Table II. For the remaining optical parameters, a series of test simulations were performed to confirm that, as expected, the parameters of the sidewall surfaces (sidewall absorptivity, α_{side}, and roughness, β_{side}) dominate the lateral spread of optical photons. For that reason, those dominant parameters were varied in a two-dimensional parameter sweep to find the combination of values that provide the best fit to the empirically determined optical MTFs for both the black and mirror top reflectors. The other applicable parameters (roughness of the top and bottom surfaces, β_{top} and β_{bot}) were kept constant at arbitrary values since variation in these values had negligible effect on the results.

TABLE II. Summary of optical parameters associated with simulations performed with the Geant4 package: absorptivity, α, roughness, β, and transmittance, τ, for the top, side, and bottom of the scintillator elements. The first two columns indicate those parameters that could, in principle, be used in the simulations. For those parameters and for each of a black and mirror top reflector, the table also indicates: the fixed value assigned to some parameters; the parameters that were irrelevant in the study ("Not applicable"); the parameters whose values have little effect upon the fitting ("Insensitive"); the range of parameter values (and increment) considered in the fitting of the empirically determined optical MTF; and the parameters whose values were calculated ("Calculated"). Finally, the values used for the refractive indices of BGO, septal wall material, and a-Si of the underlying AMFPI array are also shown.

		Black reflector	Mirror reflector
Top surface	α_{top}	1	0
	β_{top}	Not applicable	1 (Insensitive)
	τ_{top}	Not applicable	0
Side surface	α_{side}	Range: 0–0.15 (Increment: 0.01)	Range: 0–0.15 (Increment: 0.01)
	β_{side}	Range: 0–1 (Increment: 0.1)	Range: 0–1 (Increment: 0.1)
	τ_{side}	Calculated	Calculated
Bottom surface	α_{bot}	Not applicable	Not applicable
	β_{bot}	1 (Insensitive)	1 (Insensitive)
	τ_{bot}	Calculated	Calculated
Refractive index	n_{BGO}	2.15	2.15
	n_{septa}	1.55	1.55
	$n_{\text{a-Si}}$	1.7	1.7

Figure 4 shows MTF results related to the determination of the optical parameters from empirical MTF results, MTF_{sys}, obtained from the prototype BGO scintillator using the black and mirror top reflectors. The figure includes values for the various factors appearing in Eq. (1): MTF_{sys} (from Ref. 6), MTF_{rad} (from simulation), and MTF_{aper} (from calculation), as well as $\text{MTF}_{\text{opt}}^{\text{emp}}$ (obtained from these three quantities using the equation). In addition, the simulated optical MTFs, $\text{MTF}_{\text{opt}}^{\text{sim}}$, which represent the best fits to $\text{MTF}_{\text{opt}}^{\text{emp}}$ for both reflectors, are also shown. The agreement between $\text{MTF}_{\text{opt}}^{\text{sim}}$ and $\text{MTF}_{\text{opt}}^{\text{emp}}$ is seen to be good right up to the Nyquist frequency of ~0.5 mm^{-1}. The values of sidewall absorptivity α_{side} and roughness β_{side} determined from these fits are 0.08 and 0.5, respectively. Note that the optical MTFs are much lower than the upper limit represented by the aperture function which corresponds to the optical MTF of a segmented scintillator exhibiting perfect optical isolation between scintillator elements. The deduced values for the optical parameters therefore reflect the good, but less than perfect, optical isolation provided by the septal walls of the BGO prototype.

3.B. Validation of the hybrid modeling technique

In Fig. 5, simulated reconstructed images of the contrast phantom using the hybrid model, for a design representing that of the BGO prototype, are compared to corresponding

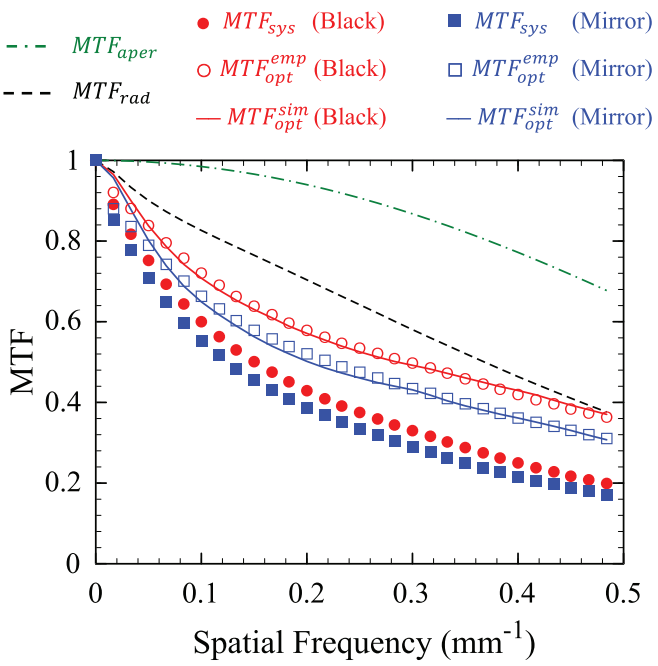

FIG. 4. Measured and simulated presampled MTF results corresponding to the prototype BGO segmented scintillator. For each of a *black* and *mirror* top reflector, results are shown for previously reported empirical results obtained from the prototype, MTF_{sys} (Ref. 6); for optical MTF values extracted from the empirical results, MTF_{opt}^{emp}; and for fits to those optical values, MTF_{opt}^{sim}. The calculated aperture function, MTF_{aper}, and simulated radiation MTF, MTF_{rad}, are also shown.

empirical images previously reported for that prototype.[11] Note that, since a mirror top reflector was used in that empirical study, all simulations of the optical gain distribution and PSF employed such a reflector. In the figure, two imaging configurations of the phantom corresponding to six different inserts are shown. In comparison with the simulated images employing only radiation transport [Fig. 5(b)], the addition of optical effects by means of the hybrid model results in images [Fig. 5(c)] that exhibit a smoother, less noisy background that is qualitatively closer to the empirical results [Fig. 5(d)].

The agreement between the simulations using the hybrid model and empirical results extends beyond visual similarity. In the case of *Contrast*, results from both radiation-only simulation and hybrid simulation provide equally good agreement with empirical results, as seen in Fig. 6. This is simply a consequence of the fact that this metric is signal-based and is determined by the attenuation properties of the object imaged, so that optical Swank noise and blur are not expected to affect it. However, for *Noise* and *CNR*, the degree of agreement between the hybrid simulation results and empirical results is much better than that between radiation-only simulation results and empirical results. This closer agreement is largely the result of the reduction in noise introduced by the optical blur in the simulated images. The good qualitative and quantitative agreement between the images obtained from the hybrid model and those obtained empirically, as demonstrated in Figs. 5 and 6, strongly supports the validity of the optical parameters used as well as the predictive capabilities of the hybrid modeling technique.

3.C. Performance evaluation of scintillator designs

Using the hybrid modeling technique, MV CBCT and spatial resolution performance for the phantom corresponding to Configuration 1 in Fig. 5 were evaluated for various hypothetical scintillator designs. For segmented scintillators with 1.016 mm pitch (corresponding to that of the prototype) and thicknesses ranging from 0.5 to 6 cm, Fig. 7 shows *Contrast*, *Noise*, and *CNR* results obtained from MV CBCT images of the phantom as well as the corresponding MTFs. As seen in

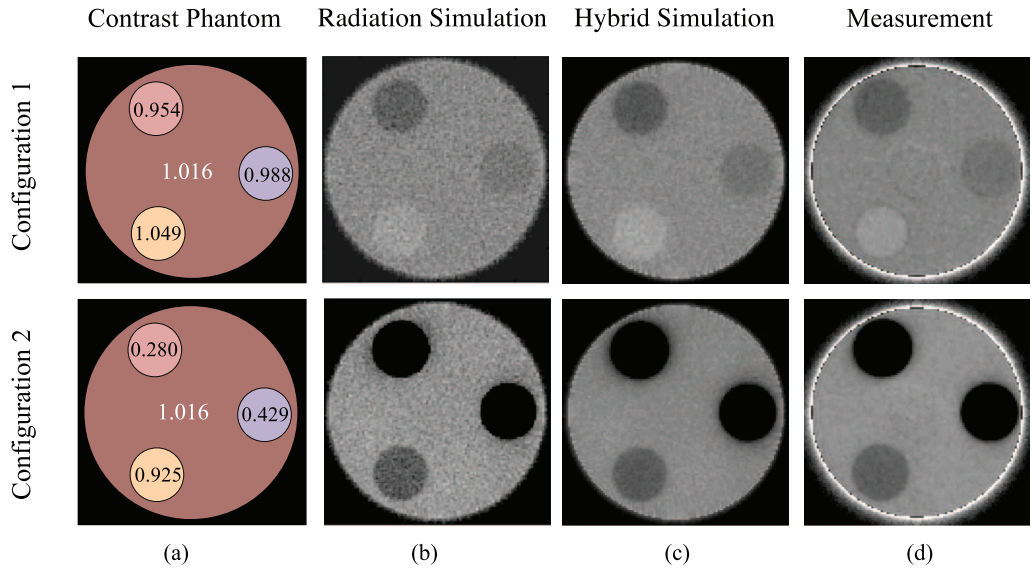

FIG. 5. Phantom information and MV CBCT images related to the prototype BGO scintillator for two phantom imaging configurations corresponding to different sets of soft-tissue inserts. (a) Values of electron densities of inserts and background relative to water. (b) Reconstructed images obtained using simulation of radiation transport only. (c) Reconstructed images obtained using the hybrid model. (d) Reconstructed images from a previous empirical study (Ref. 11). All reconstructed images were acquired at a dose of 4 cGy.

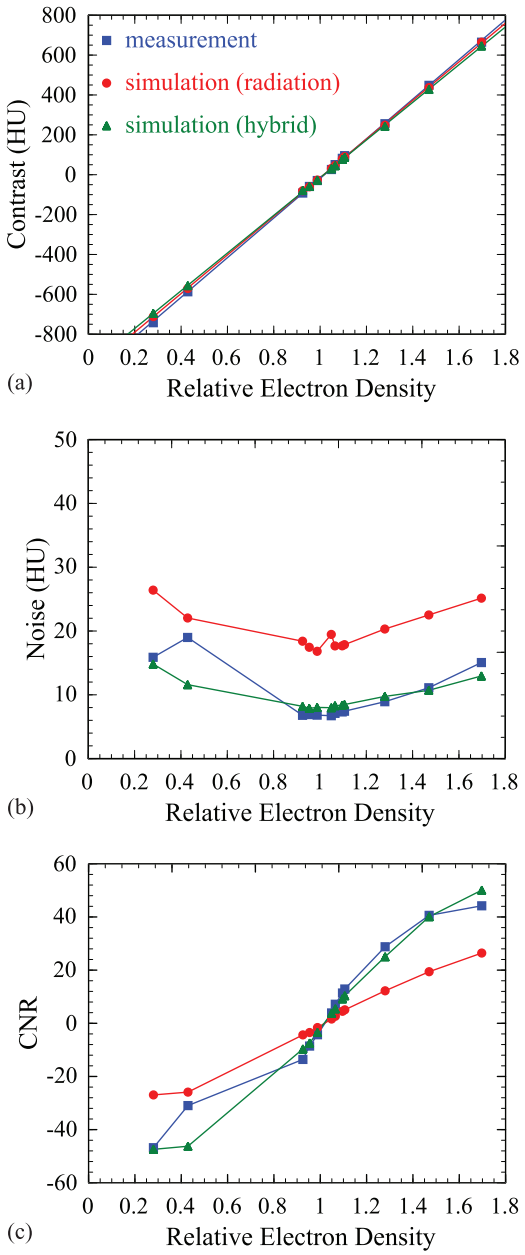

FIG. 6. Results related to the prototype BGO scintillator for four phantom imaging configurations corresponding to 12 different soft-tissue inserts (see Table I) for (a) *Contrast*, (b) *Noise*, and (c) *CNR*. The results shown were obtained from simulations employing radiation transport only (circle symbols), from simulations using the hybrid model (triangle symbols), and from a previous empirical study (Ref. 11) (square symbols). Note that, as previously reported (Ref. 11), the empirical result for each of *Noise* and *CNR* at a relative electron density of 0.429 is anomalous compared to the overall trend of the remainder of the dataset.

Fig. 7(a), thicker scintillators result in a slightly shallower slope in the plot of *Contrast* versus relative electron density of the inserts, due to a small reduction in the *absolute* values of contrast. Such diminution of contrast is probably the result of additional background scatter in the projection images caused by a higher probability of reabsorption of recoil Compton x rays for thicker scintillators. As seen in Fig. 7(b), thicker scintillators exhibit lower *Noise* as a result of the increase in the number of quanta sampled due to improved x-ray detection efficiency and increased optical blur. As a consequence, thicker scintillators provide a steeper *CNR*-slope (and therefore better soft tissue visualization), as seen in Fig. 7(c). However, thicker scintillators also suffer from reduced MTF, as seen in Fig. 7(d), due to more pronounced lateral spread of both radiation energy deposition and optical photons in the scintillator.

A similar performance evaluation was performed for segmented scintillators with a thickness of 1.13 cm (corresponding to that of the prototype) and element pitches ranging from 0.508 to 1.524 mm, and the results are shown in Fig. 8. For *Contrast*, the dependence on element pitch is almost negligible, with only a small deviation apparent at a pitch of 1.524 mm, as seen in Fig. 8(a). This deviation may be the result of larger statistical variations of *Contrast* due to a smaller number of voxels used in the regions of interest. For *Noise*, scintillators with a larger pitch exhibit lower *Noise* levels, as seen in Fig. 8(b), due to the larger number of quanta collected by a given element and the reduced optical Swank noise contribution due to a smaller aspect ratio of the crystals.[13] As a consequence, scintillators with larger pitch provide steeper *CNR*-slope, as seen in Fig. 8(c), leading to better soft-tissue visualization. However, as expected, scintillators with larger pitch also exhibit degraded spatial resolution characterized by lower MTF, as seen in Fig. 8(d).

3.D. Optimization of scintillator design

The complexities of how scintillator design affects CNR and spatial resolution performance makes it of interest to identify those regions in the continuum of design offering the best achievable combination of CNR and MTF (referred to as optimum performance in this paper). Toward this objective, these two performance metrics were determined using the hybrid model for scintillator designs with pitches ranging from 0.508 to 1.524 mm and thicknesses ranging from 0.5 to 6 cm, and the results are shown in the form of bar charts in Figs. 9(a) and 9(b). As seen in Fig. 9(a), the behavior of *CNR*-slope with increasing thickness is complex. For pitches 1.016 mm and greater, *CNR*-slope increases throughout the range, but with diminishing returns beyond ~3 cm. For smaller pitches of 0.508 and 0.762 mm, *CNR*-slope increases up to thicknesses of ~4 and 5 cm, respectively, before slightly decreasing—a result of the significant contribution of optical Swank noise for designs with high aspect ratio crystals. The behavior of spatial resolution, defined in this instance as the spatial frequency at which MTF drops to 0.5 (f_{50}), is simpler, as observed in Fig. 9(b). For all pitches considered, performance degrades with increasing thickness in an asymptotic manner.

A method for finding regions of design offering optimum performance is illustrated in Fig. 9(c), where contour lines of iso-*CNR*-slope and iso-f_{50} are plotted, based upon the results reported in Figs. 9(a) and 9(b) and employing a spline interpolation between data points. In the figure, the iso-*CNR*-slope lines represent values ranging from 39.5 to 235.9 at intervals of 10.3 while the iso-f_{50} lines represent values ranging from 0.0736 to 0.2101 mm^{-1} at intervals of 0.00455 mm^{-1}. (Note that the arrows superimposed on the contour lines indicate the

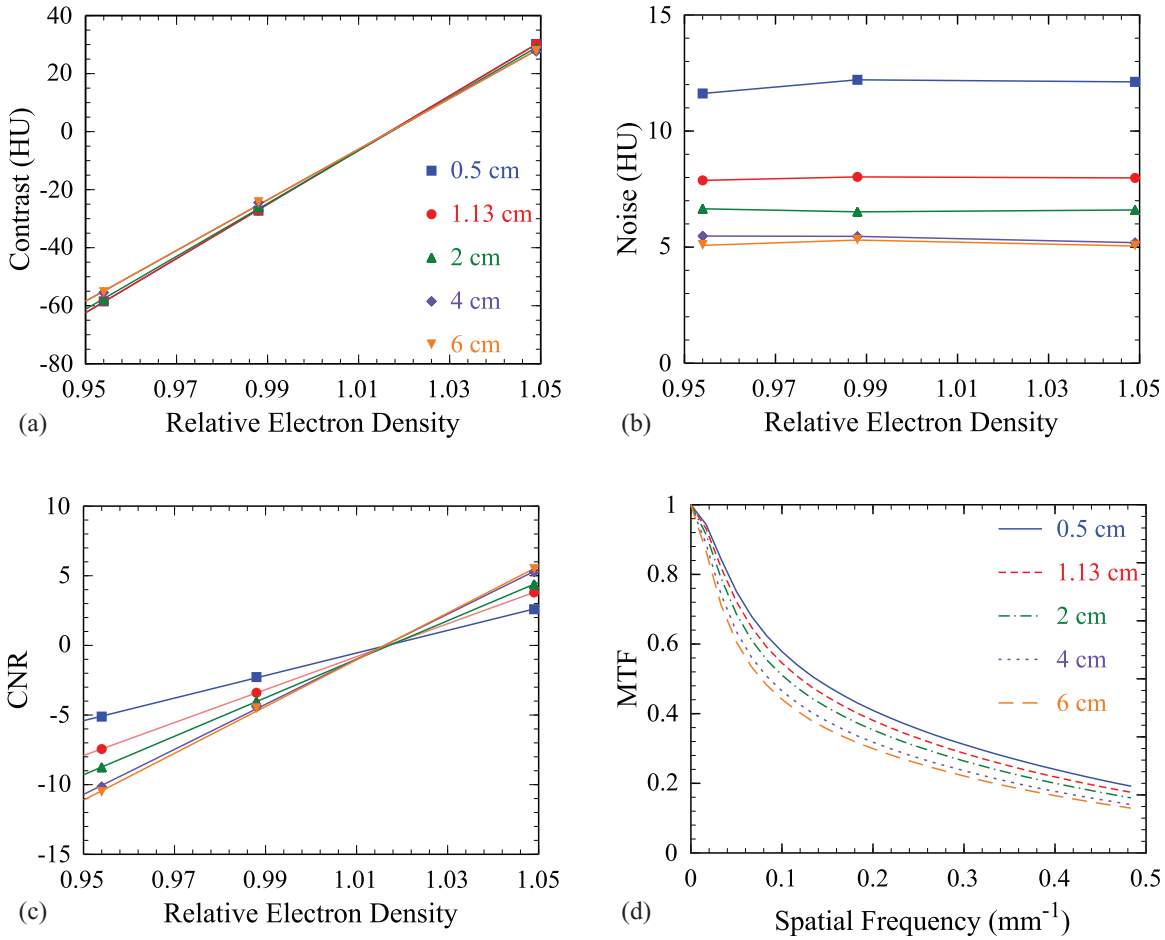

FIG. 7. Simulation results obtained using the hybrid model for hypothetical 1.016 mm pitch BGO scintillator designs with varying thicknesses for (a) *Contrast*, (b) *Noise*, and (c) *CNR*. The results are plotted as a function of electron density of tissue-equivalent inserts relative to water. (d) Simulated results for MTF for those designs. Note that the lines appearing in the *Contrast* and *CNR* plots represent linear fits to the results.

direction of increasing value for each of *CNR*-slope and f_{50}.) The determination of optimum performance entailed finding the location corresponding to the highest value of f_{50} along a given line of iso-*CNR*-slope or, equivalently, finding the location corresponding to the highest value of *CNR*-slope along a given line of iso-f_{50}. The degree of optimization (i.e., proximity to optimum performance) is indicated by means of a color spectrum where hotter colors represent regions of superior performance. In this color map, results were presented only up to a thickness of 3 cm since, for larger thicknesses, regions of optimum performance occur at pitches larger than the upper limit of 1.524 mm.

Information of the type given in Fig. 9(c) provides insight that can guide decision-making in scintillator design. For example, at an element pitch of 0.8 mm (which approximately corresponds to the pitch presently used in conventional MV AMFPIs), optimum performance is achieved for a scintillator thickness of ~0.9 cm. For thicker scintillators employing the same pitch of 0.8 mm, the improvement in *CNR*-slope is relatively minor whereas the degradation in spatial resolution is more significant, as indicated by the shallower slopes of the iso-*CNR*-slope lines compared to the steeper slopes of the iso-f_{50} lines. The map also illustrates the impact of a tradeoff between element pitch and scintillator thickness. For example, while a scintillator design with a pitch of ~0.72 mm and a thickness of 3 cm (indicated by a circle symbol) provides the same f_{50} as a design with a pitch of 1.016 mm and a thickness of ~1.13 cm (indicated by a star symbol and corresponding to the BGO prototype), *CNR* performance is slightly inferior, as indicated by the corresponding contour lines. This demonstrates that choosing a much thicker (and thus more costly) scintillator to improve x-ray detection efficiency, while reducing pitch to preserve spatial resolution, is not necessarily an effective strategy.

The results of a parallel analysis involving simulation of radiation transport only—conceptually corresponding to the performance of "ideal" scintillators exhibiting no optical Swank noise or optical blur—are shown in Figs. 9(d)–9(f). In this case, compared to the results shown in Figs. 9(a) and 9(b), the values appearing in Figs. 9(d) and 9(e) are systematically lower for *CNR*-slope and higher for f_{50}, largely due to the absence of optical blur. Also, the behavior of *CNR*-slope with increasing thickness demonstrates a much simpler trend, consisting of a monotonic increase with diminishing returns beyond ~3 cm. In the optimization map shown in Fig. 9(f), the iso-*CNR*-slope lines represent levels ranging from 19.8 to 110.7 at intervals of 4.55, and iso-f_{50} lines represent levels ranging from 0.258 to 0.535 mm^{-1} at intervals of 0.00925

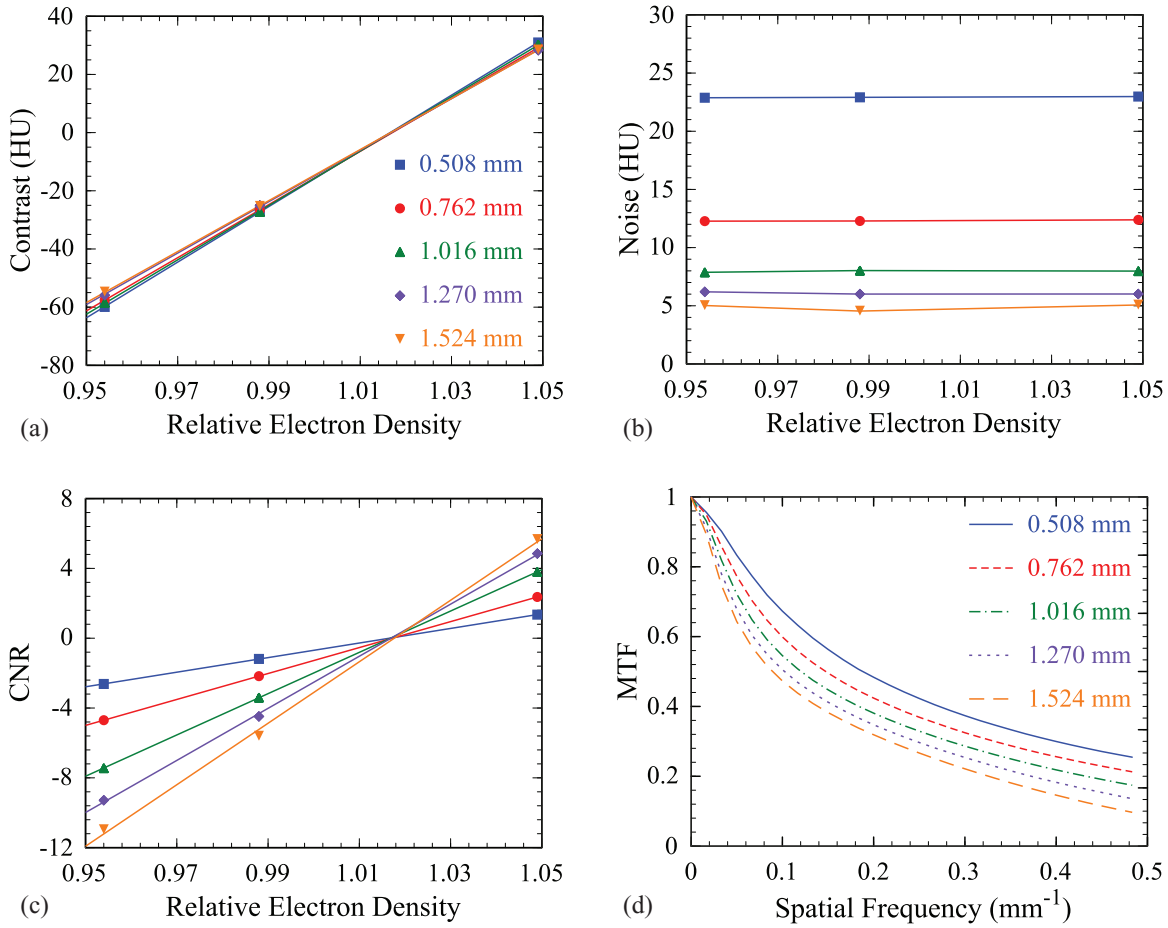

FIG. 8. Simulation results obtained using the hybrid model for hypothetical 1.13 cm thick BGO scintillator designs with varying element pitches for (a) *Contrast*, (b) *Noise*, and (c) *CNR*. The results are plotted as a function of electron density of tissue-equivalent inserts relative to water. (d) Simulated results for MTF for those designs. Note that the lines appearing in the *Contrast* and *CNR* plots represent linear fits to the results.

mm^{-1}. Compared to the results shown in Fig. 9(c), the map in Fig. 9(f) exhibits a noticeably different pattern for optimum performance—with thicker scintillators more strongly favored for pitches greater than ~0.9 mm. Note that from an examination of the individual contributions of optical Swank noise and optical blur, it is found that both effects significantly contribute to shifting optimum performance toward thinner scintillator designs. For Swank noise, this outcome is simply due to an accelerating decrease in CNR-slope as scintillator thickness increases. In the case of blur, it is a consequence of opposing trends of more significant degradation of spatial resolution compared to relatively moderate improvement of CNR-slope as scintillator thickness increases. Comparison of results which are based on simulations employing optical parameters obtained from actual prototypes [such as those in Fig. 9(c)], with results which correspond to optically ideal scintillators [such as those in Fig. 9(f)], can provide valuable insight for improving the optical properties of segmented scintillator designs.

4. DISCUSSION

Thick, segmented scintillators represent a promising replacement for the type of phosphor screens employed in current MV AMFPIs for radiation therapy by virtue of offering order of magnitude improvement in DQE. This significant improvement greatly facilitates soft-tissue visualization at low dose using MV CBCT. In order to maximize the clinical benefit of these scintillators, it is important to optimize their performance through judicious choice of design parameters such as scintillator thickness and element pitch. Toward achieving this goal, a theoretical study exploring the performance of various BGO scintillator designs in terms of contrast-to-noise ratio and modulation transfer function has been reported. The study employs a novel hybrid modeling technique which takes into account both radiation and optical effects.

For a given scintillator design, the hybrid technique employs images obtained from Monte Carlo simulation of radiation transport in combination with an optical gain distribution and PSF obtained from Monte Carlo simulation of optical transport. While parameter values for the radiation transport simulation are readily available, those for optical transport need to be determined for the scintillator material, side surfaces (i.e., septal walls), as well as top and bottom surfaces of the crystal elements. These optical parameter values could, in principle, be determined using direct, independent optical measurements on each component, although the multitude of surface properties (absorptivity, roughness,

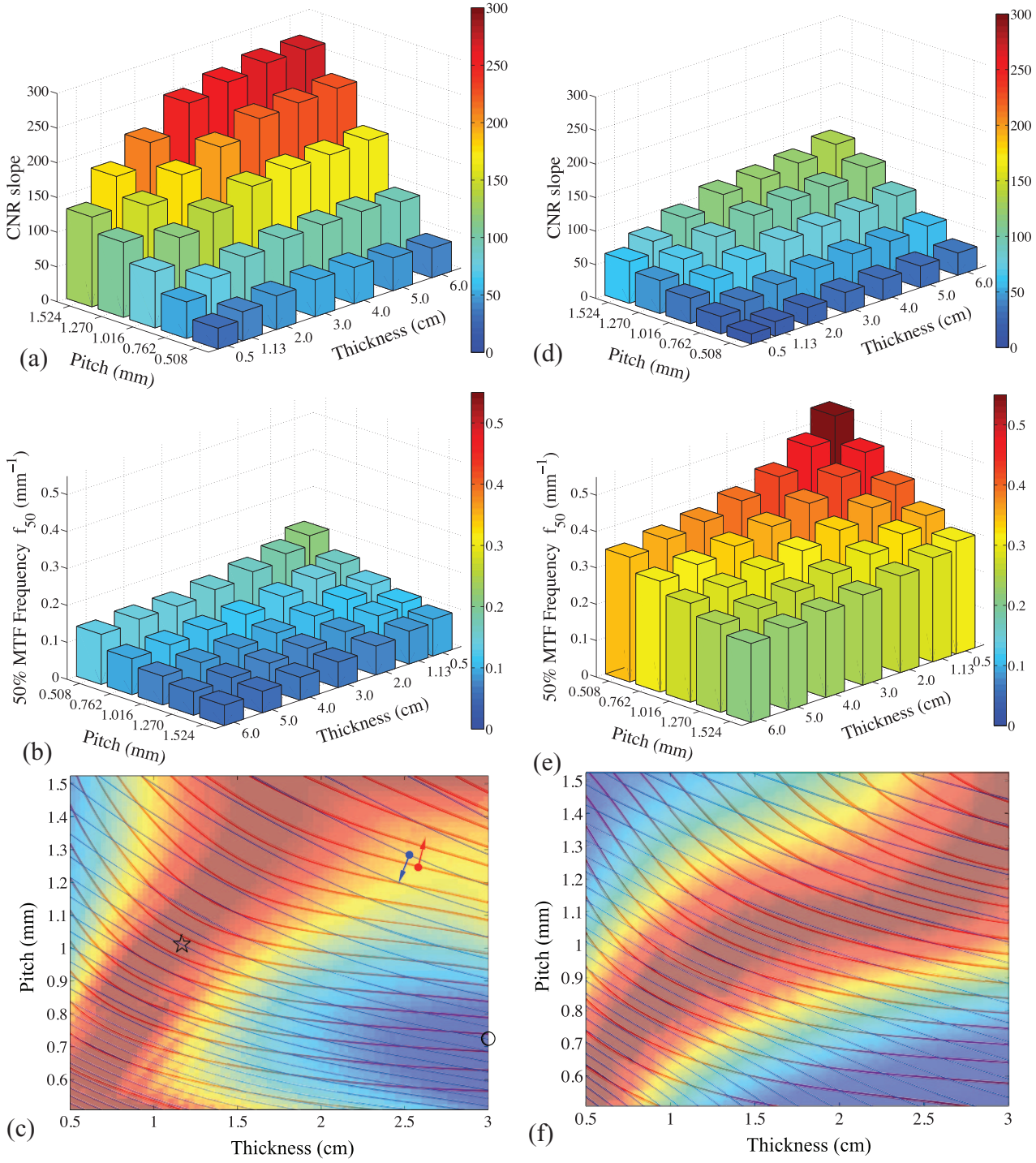

FIG. 9. Simulation results obtained using the hybrid model for (a) *CNR*-slope, (b) 50% MTF frequency, f_{50}, and (c) contour lines of iso-*CNR*-slope (red lines) and iso-f_{50} (blue lines) along with an overlying optimization map, as a function of the pitch and thickness of various hypothetical scintillator designs. Corresponding results obtained using radiation transport simulation only are plotted in (d)–(f). Note that, for purposes of enhanced presentation, the direction for increasing values of element pitch and scintillator thickness is reversed between the *CNR*-slope and f_{50} plots.

and transmittance) that needs to be considered constitutes a challenge. In this paper, realistic values for these parameters were obtained through fitting simulated optical MTFs to their empirical counterparts which were extracted from measured results obtained from a prototype BGO segmented scintillator with a thickness of ~1.13 cm. Of course, these values are specific to the form of the optical model chosen for the current study—so that changes to the model could result in different sets of parameters and values.

The inclusion of optical effects by means of a simulated optical gain distribution and PSF, as opposed to directly simulating the transport of the individual optical photons generated by each x ray interacting in the scintillator, offers a number of advantages. The consolidation of optical transport into a

single optical simulation that is decoupled from the radiation transport results in significant reduction in the computational time per design required for the optical simulations—which allows examination of a far greater range of scintillator designs than would otherwise be practical. This reduction originates from the fact that the time necessary for simulating an optical gain distribution and PSF is dose-independent, requiring only on the order of 10^8 optical photon histories per design, whereas the time needed to perform a conventional Monte Carlo optical transport simulation scales linearly with the dose in addition to requiring a number of optical photon histories consistent with the light yield of the scintillator. Another advantage of decoupling the optical effects from the radiation transport is the flexibility of performing repeated calculations of the optical gain distribution and PSF (for example, to examine the effect of varying the values of the optical parameters) without having to repeat the radiation simulation.

In this study, the rectangular cuboid crystal shape assumed for the various hypothetical scintillator designs was chosen since it is considerably more practical to manufacture than focused shapes. However, this makes the reported performance results subject to the effects of beam divergence.[14,15] While those effects are generally small as a result of the relatively limited detection area considered in the simulations (which restricted the maximum divergence angle to 3°), they nevertheless do contribute to more lateral spread of radiation energy. For locations further off the central beam axis, divergence effects would of course be more pronounced, reducing MTF (particularly for thicker detectors), and leaving *CNR* unaffected since noise is not affected by beam divergence.[14,15] In this case, regions of optimum performance would be shifted toward thinner scintillators than those indicated in Fig. 9(c)—due to significant degradation of spatial resolution.[14,15] However, the use of focused scintillators would largely restore spatial resolution,[15] resulting in a performance optimization map similar to that of Fig. 9(c).

While the present study focuses on two-dimensional matrices of optically isolated scintillating crystals for CBCT imaging at 6 MV, the hybrid modeling technique described in this paper could be applied to other situations. For example, it would be anticipated that optimization of such detectors for lower megavoltage energies realized through use of low-Z target materials[43–46] would favor designs with thinner crystals. Alternatively, the methodology could be applied toward the design of detectors required for other imaging geometries, such as fan-beam configurations of the type used in Tomotherapy treatment machines. In this case, the reduced level of scattered radiation would also be expected to favor thinner crystals.

It is interesting to note how the optical parameters employed in this study affect scintillator performance. For example, the 8% absorption efficiency used in the study has a detrimental effect on optical Swank noise for thicker scintillators since Swank noise is highly dependent on the efficiency of light transport within the scintillator. Another example is that light transmission through septal walls results in progressively more spatial resolution degradation as scintillator thickness increases. Both wall absorption and transmission diminish the benefit of improved quantum detection efficiency provided by thicker scintillators, prompting the need for careful performance optimization of scintillator design. For segmented scintillators with highly transparent crystals, relatively low absorption in the septal walls, and a low aspect ratio for the crystals, optical Swank noise has negligible effect on total image noise. This situation applies in the case of the prototype BGO scintillator, since BGO material has an optical mean free path length of ~30 cm and the prototype has a crystal aspect ratio of only ~11. Therefore, for this prototype, the inclusion of optical Swank noise in the hybrid modeling technique had a minor effect on the simulation results, as is demonstrated by the close agreement between the simulated and empirical noise performance—an agreement that is largely a result of the inclusion of optical blur. For designs with thicker scintillators (up to 6 cm) and smaller pitches (down to 0.508 mm), the corresponding increase in the aspect ratio of the crystals significantly increases Swank noise[13]—resulting in a less pronounced increase in CNR as a function of increasing scintillator thickness, and even a decrease of CNR for designs with the largest aspect ratios. For segmented scintillators with better septal wall properties (i.e., lower absorption and lower transmission), the effects of Swank noise and optical blur are expected to be less important, resulting in a performance optimization that would more closely approach the ideal scintillator behavior shown in Fig. 9(f).

In the current study, the use of the MTF metric associated with 2D imaging system spatial resolution provided a computationally practical means to evaluate the performance of hypothetical segmented scintillator designs—in the spirit of providing insight about how the trade-offs in contrast-to-noise ratio and resolution are affected by basic design parameters. Beyond this study, it would be instructive to examine the effect of scintillator design upon 3D spatial resolution—which would entail accounting for factors beyond the pitch and thickness of the scintillator. Previous empirical and theoretical investigations of 3D spatial resolution for CBCT systems have demonstrated that 3D MTF depends upon many factors such as: the details of the reconstruction algorithm (including the choice of filter), the voxel size, the number of projection images, the magnification factor, the position and direction of MTF analysis within the reconstructed volume, and scatter from the phantom or patient.[47–49] Depending upon the decisions made to account for these many additional details, the shape of the resulting optimization maps compared to those of the present study could well be affected. Finally, it should be noted that the computation time required for such a simulation study of 3D resolution would, of itself, be significantly greater than that of the entire present study.

ACKNOWLEDGMENTS

The authors would like to thank Dr. Ian Cunningham for insightful discussions and Richard Choroszucha for help with the implementation of the reconstruction algorithm. This project was supported in part by NIH Grant No. R01 CA051397.

[a]Author to whom correspondence should be addressed. Electronic mail: antonuk@umich.edu; Telephone: 734-936-4312; Fax: 734-936-2261.

[1]L. E. Antonuk, "Electronic portal imaging devices: A review and historical perspective of contemporary technologies and research," Phys. Med. Biol. **47**, R31–R65 (2002).

[2]P. Munro and D. C. Bouius, "X-ray quantum limited portal imaging using amorphous silicon flat-panel arrays," Med. Phys. **25**, 689–707 (1998).

[3]Y. El-Mohri, K-W Jee, L. E. Antonuk, M. Maolinbay, and Q. Zhao, "Determination of the detective quantum efficiency of a prototype, megavoltage indirect detection, active matrix flat-panel imager," Med. Phys. **28**, 2538–2550 (2001); L. E. Antonuk, Y. El-Mohri, and Y. Wang, *ibid.* **33**, 251 (2006) (Erratum).

[4]A. L. Boyer, L. E. Antonuk, A. Fenster, M. Van Herk, H. Meertens, P. Munro, L. E. Reinstein, and J. Wong, "A review of electronic portal imaging devices (EPIDs)," Med. Phys. **19**, 1–16 (1992).

[5]P. M. Evans, "Anatomical imaging for radiotherapy," Phys. Med. Biol. **53**, R151–R191 (2008).

[6]Y. Wang, L. E. Antonuk, Q. Zhao, Y. El-Mohri, and L. Perna, "High-DQE EPIDs based on thick, segmented BGO and CsI:Tl scintillators: Performance evaluation at extremely low dose," Med. Phys. **36**, 5707–5718 (2009).

[7]P. Munro, "Megavoltage radiography for treatment verification," in *The Modern Technology of Radiation Oncology—A Compendium for Medical Physicists and Radiation Oncologists*, edited by J. V. Dyk (Medical Physics Publishing, Madison, WI, 1999), pp. 481–508.

[8]J. Sillanpaa, J. Chang, G. Mageras, E. Yorke, F. De Arruda, K. Rosenzweig, P. Munro, E. Seppi, J. Pavkovich, and H. Amols, "Low-dose megavoltage cone-beam computed tomography for lung tumors using a high-efficiency image receptor," Med. Phys. **33**, 3489–3497 (2006).

[9]A. Sawant, L. E. Antonuk, Y. El-Mohri, Q. Zhao, Y. Wang, Y. Li, H. Du, and L. Perna, "Segmented crystalline scintillators: Empirical and theoretical investigation of a high quantum efficiency EPID based on an initial engineering prototype CsI(Tl) detector," Med. Phys. **33**, 1053–1066 (2006).

[10]P. F. Kirvan, T. T. Monajemi, B. G. Fallone, and S. Rathee, "Performance characterization of a MVCT scanner using multislice thick, segmented cadmium tungstate-photodiode detectors," Med. Phys. **37**, 249–257 (2010).

[11]Y. El-Mohri, L. E. Antonuk, Q. Zhao, R. B. Choroszucha, H. Jiang, and L. Liu, "Low-dose megavoltage cone-beam CT imaging using thick, segmented scintillators," Phys. Med. Biol. **56**, 1509–1527 (2011).

[12]Y. Wang, L. E. Antonuk, Y. El-Mohri, Q. Zhao, A. Sawant, and H. Du, "Monte Carlo investigations of megavoltage cone-beam CT using thick, segmented scintillating detectors for soft tissue visualization," Med. Phys. **35**, 145–158 (2008).

[13]Y. Wang, L. E. Antonuk, Y. El-Mohri, and Q. Zhao, "A Monte Carlo investigation of Swank noise for thick, segmented, crystalline scintillators for radiotherapy imaging," Med. Phys. **36**, 3227–3238 (2009).

[14]Y. Wang, Y. El-Mohri, L. E. Antonuk, and Q. Zhao, "Monte Carlo investigations of the effect of beam divergence on thick, segmented crystalline scintillators for radiotherapy imaging," Phys. Med. Biol. **55**, 3659–3673 (2010).

[15]L. Liu, L. E. Antonuk, Q. Zhao, Y. El-Mohri, and H. Jiang, "Countering beam divergence effects with focused segmented scintillators for high DQE megavoltage active matrix imagers," Phys. Med. Biol. **57**, 5343–5358 (2012).

[16]D. Constantin, M. Sun, E. Abel, J. Star-Lack, and R. Fahrig, "Coupled radiative and optical Geant4 simulation of MV EPIDs based on thick pixelated scintillating crystals," Med. Phys. **39**, 3951–3952 (2012).

[17]J. Pouliot, A. Bani-Hashemi, J. Chen, M. Svatos, F. Ghelmansarai, M. Mitschke, M. Aubin, P. Xia, O. Morin, K. Bucci, M. Roach III, P. Hernandez, Z. Zheng, D. Hristov, and L. Verhey, "Low-dose megavoltage cone-beam CT for radiation therapy," Int. J. Radiat. Oncol., Biol., Phys. **61**, 552–560 (2005).

[18]O. Morin, A. Gillis, J. Chen, M. Aubin, M. K. Bucci, M. Roach III, and J. Pouliot, "Megavoltage cone-beam CT: System description and clinical applications," Med. Dosim. **31**, 51–61 (2006).

[19]M. Aubin, O. Morin, J. Chen, A. Gillis, B. Pickett, J. F. Aubry, C. Akazawa, J. Speight, M. Roach III and J. Pouliot, "The use of megavoltage cone-beam CT to complement CT for target definition in pelvic radiotherapy in the presence of hip replacement," Br. J. Radiol. **79**, 918–921 (2006).

[20]H. Guan, F. F. Yin, and J. H. Kim, "Accuracy of inhomogeneity correction in photon radiotherapy from CT scans with different settings," Phys. Med. Biol. **47**, N223–N231 (2002).

[21]K. M. Langen, S. L. Meeks, D. O. Poole, T. H. Wagner, T. R. Willoughby, P. A. Kupelian, K. J. Ruchala, J. Haimerl, and G. H. Olivera, "The use of megavoltage CT (MVCT) images for dose recomputations," Phys. Med. Biol. **50**, 4259–4276 (2005).

[22]O. Morin, J. Chen, M. Aubin, A. Gillis, J.-F. Aubry, S. Bose, H. Chen, M. Descovich, P. Xia, and J. Pouliot, "Dose calculation using megavoltage cone-beam CT," Int. J. Radiat. Oncol., Biol., Phys. **67**, 1201–1210 (2007).

[23]T. T. Monajemi, S. Steciw, B. G. Fallone, and S. Rathee, "Modeling scintillator-photodiodes as detectors for megavoltage CT," Med. Phys. **31**, 1225–1234 (2004).

[24]P. M. Evans, M. A. Mosleh-Shirazi, E. J. Harris, and J. Seco, "Monte Carlo and Lambertian light guide models of the light output from scintillation crystals at megavoltage energies," Med. Phys. **33**, 1797–1809 (2006).

[25]T. T. Monajemi, B. G. Fallone, and S. Rathee, "Thick, segmented $CdWO_4$-photodiode detector for cone beam megavoltage CT: A Monte Carlo study of system design parameters," Med. Phys. **33**, 4567–4577 (2006).

[26]Y. El-Mohri, L. E. Antonuk, R. B. Choroszucha, Q. Zhao, H. Jiang, and L. Liu, "Optimization of the performance of segmented scintillators for radiotherapy imaging through novel binning techniques," Phys. Med. Biol. **59**, 797–818 (2014).

[27]G. F. Knoll, *Radiation Detection and Measurement* (Wiley, Hoboken, NJ, 2010).

[28]M. F. Fast, T. Koenig, U. Oelfke, and S. Nill, "Performance characteristics of a novel megavoltage cone-beam-computed tomography device," Phys. Med. Biol. **57**, N15–N24 (2012).

[29]D. Létourneau, J. W. Wong, M. Oldham, M. Gulam, L. Watt, D. A. Jaffray, J. H. Siewerdsen, and A. A. Martinez, "Cone-beam-CT guided radiation therapy: Technical implementation," Radiother. Oncol. **75**, 279–286 (2005).

[30]J. Siewerdsen, M. Daly, B. Bakhtiar, D. Moseley, S. Richard, H. Keller, and D. Jaffray, "A simple, direct method for x-ray scatter estimation and correction in digital radiography and cone-beam CT," Med. Phys. **33**, 187–197 (2006).

[31]M. Loubele, F. Maes, R. Jacobs, D. van Steenberghe, S. White, and P. Suetens, "Comparative study of image quality for MSCT and CBCT scanners for dentomaxillofacial radiology applications," Radiat. Prot. Dosim. **129**, 222–226 (2008).

[32]N. Mail, D. Moseley, J. Siewerdsen, and D. Jaffray, "The influence of bowtie filtration on cone-beam CT image quality," Med. Phys. **36**, 22–32 (2009).

[33]C. Beltran, R. Lukose, B. Gangadharan, A. Bani-Hashemi, and B. A. Faddegon, "Image quality & dosimetric property of an investigational imaging beam line MV-CBCT," J. Appl. Clin. Med. Phys. **10**, 37–48 (2009).

[34]C. Ling, P. Zhang, T. Etmektzoglou, J. Star-lack, M. Sun, E. Shapiro, and M. Hunt, "Acquisition of MV-scatter-free kilovoltage CBCT images during RapidArc™ or VMAT," Radiother. Oncol. **100**, 145–149 (2011).

[35]D. Sheikh-Bagheri, Ph.D. thesis, Carleton University, 1999.

[36]H. Fujita, D. Tsai, T. Itoh, K. Doi, J. Morishita, K. Ueda, and A. Ohtsuka, "A simple method for determining the modulation transfer function in digital radiography," IEEE Trans. Med. Imaging **11**, 34–39 (1992).

[37]R. K. Swank, "Absorption and noise in x-ray phosphors," J. Appl. Phys. **44**, 4199–4203 (1973).

[38]I. Kawrakow and D. W. O. Rogers, "The EGSnrc code system: Monte Carlo simulation of electron and photon transport," Technical Report PIRS-701 (National Research Council of Canada, Ottawa, Canada, 2000).

[39]I. Kawrakow, "egspp: The EGSnrc C++ class library," Technical Report PIRS-899 (National Research Council of Canada, Ottawa, Canada, 2005).

[40]S. Agostinelli *et al.*, "GEANT4–a simulation toolkit," Nucl. Instrum. Methods Phys. Res. A **506**, 250–303 (2003).

[41]P. Lecoq, P. Li, and B. Rostaing, "BGO radiation damage effects: Optical absorption, thermoluminescence and thermoconductivity," Nucl. Instrum. Methods Phys. Res. A **300**, 240–258 (1991).

[42]M. Born and E. Wolf, "Principles of optics: Electromagnetic theory of propagation, interference and diffraction of light," CUP Archive, 1999.

[43]B. A. Faddegon, V. Wu, J. Pouliot, B. Gangadharan, and A. Bani-Hashemi, "Low dose megavoltage cone beam computed tomography with an unflattened 4 MV beam from a carbon target," Med. Phys. **35**, 5777–5786 (2008).

[44]R. T. Flynn, J. Hartmann, A. Bani-Hashemi, E. Nixon, R. Alfredo, C. Siochi, E. C. Pennington, and J. E. Bayouth, "Dosimetric characterization and application of an imaging beam line with a carbon electron target

for megavoltage cone beam computed tomography," Med. Phys. **36**, 2181–2192 (2009).
[45]J. L. Robar, T. Connell, W. Huang, and R. G. Kelly, "Megavoltage planar and cone-beam imaging with low-Z targets: Dependence of image quality improvement on beam energy and patient separation," Med. Phys. **36**, 3955–3963 (2009).
[46]D. Sawkey, M. Lu, O. Morin, M. Aubin, S. Yom, A. Gottschalk, A. Bani-Hashemi, and B. Faddegon, "A diamond target for megavoltage cone-beam CT," Med. Phys. **37**, 1246–1253 (2010).
[47]A. L. C. Kwan, J. M. Boone, K. Yang, and S.-Y. Huang, "Evaluation of the spatial resolution characteristics of a cone-beam breast CT scanner," Med. Phys. **34**, 275–281 (2007).
[48]K. Yang, A. L. C. Kwan, and J. M. Boone, "Computer modeling of the spatial resolution properties of a dedicated breast CT system," Med. Phys. **34**, 2059–2069 (2007).
[49]J.-P. Bissonnette, D. J. Moseley, and D. A. Jaffray, "A quality assurance program for image quality of cone-beam CT guidance in radiation therapy," Med. Phys. **35**, 1807–1815 (2008).